ADVANCED PHYSICS RESEARCH

Open Access

Supporting Information

Spontaneous Electric Polarization in Graphene Polytypes

Simon Salleh Atri, Wei Cao, Bar Alon, Nirmal Roy, Maayan Vizner Stern, Vladimir Falko, Moshe Goldstein, Leeor Kronik, Michael Urbakh, Oded Hod and Moshe Ben Shalom*

Spontaneous Electric Polarization in Graphene Polytypes

Supplementary Information.

Table of Contents

S1. Crystalline Polytypes of Multilayer Graphene

The term polytype refers to any of a number of forms of a crystalline substance, the arrangement of which differs only along one of the unit-cell dimensions. In bilayer graphene, given that the fully eclipsed high-symmetry AA stacking configuration is unstable, there is one polytype with two equivalent stacking configurations, namely AB and BA. The same logic follows for N-layered graphitic stacks, where only a part of the possible 2^{N-1} high-symmetry stacking configurations accessible through layer sliding exhibit distinct dispersion relations.

To count the number of distinguishable crystals and to identify the polarization properties of each polytype, it is instructive to classify them according to their inversion (I) (x→-x, y→-y, z→-z) and mirror (M) (z→-z) symmetries. If a point in space exists for which (I) results in the same structure, the system is non-polar. If I is broken, permanent in-plane polarization may emerge for M-symmetric structures. Additional out-of-plane polarization may be found if the M symmetry is also broken.

We note that for AB/BA stacking:

a. Polytypes with no I and no M symmetry have four equivalent stacking configurations, obtained from one polytype by applying I, M, or I and M operations.

b. Polytypes with either I or M have two degenerate stacking configurations, obtained from one polytype by applying the I or M operation.
c. There are no polytypes with both I and M.

For example, in tri-layers $N=3$ and there are $2^{3-1}=4$ possible stacking configurations, but only two distinct polytypes: B (M symmetric) and R (I symmetric). In tetra layers, $N=4$, the B and R polytypes are I symmetric (and therefore each is counted twice according to the above rules), while the P polytype breaks both I and M and hence is counted four times. Subtracting the over-counted configuration degeneracies out of the total of $2^{4-1}=8$ configurations, we find that there remain only 8-1-1-3=3 unique polytypes: B, R, and P.

We further note that if the number of layers N is even, then no polytypes are M symmetric due to the shift at the middle interfacial plane, and $2^{(N-2)/2}$ polytypes are I symmetric. To see this, consider fixing the inversion point between the eclipsed atoms of the two middle layers (see Fig. 1b,c in the main text) and only counting the number of stacking options above the middle plane. The stacking configurations below the middle plane are then fixed to conserve I. Hence, they do not add new configurations to the count. If the number of layers N is odd, then $2^{(N-3)/2}$ polytypes are M symmetric, and $2^{(N-3)/2}$ polytypes are I symmetric. To see this, consider fixing the inversion point between the two atoms of the middle layer and counting the number of stacking options above it only. The stacking configuration below is then fixed to either conserve I or conserve M and hence does not introduce new polytypes to the count.

To summarize, for even/odd N:

a. $2^{(N-2)/2}$ / $2^{(N-3)/2}$ polytypes are I symmetric (and must break M symmetry). These polytypes are not polar.

b. 0 / $2^{(N-3)/2}$ polytypes break I symmetry but conserve M symmetry. These polytypes are polar in plane only.

c. All remaining polytypes, the number of which is $\frac{1}{4}(2^{(N-1)} - 2\times 2^{(N-2)/2})$ / $\frac{1}{4}(2^{(N-1)} - 2\times 2\times 2^{(N-3)/2})$, break both I and M symmetries and can be polar both in and out of the plane.

Table 1 summarizes the above combinatorial count for $N=2$ to 20. For example, it shows that there are 136 distinct polytypes for ten layers and 131,328 distinct polytypes for 20 layers. As also shown in the Table, most of these configurations exhibit broken I and M symmetry and therefore support out-of-plane polarization.

N	No P (I Mz)	IP P (I Mz)	OOP+IP (I Mz)	Total
2	1	0	0	1
3	1	1	0	2
4	2	0	1	3
5	2	2	2	6
6	4	0	6	10
7	4	4	12	20
8	8	0	28	36
9	8	8	56	72
10	16	0	120	136
11	16	16	240	272
12	32	0	496	528
13	32	32	992	1056
14	64	0	2016	2080
15	64	64	4032	4160
16	128	0	8128	8256
17	128	128	16256	16512
18	256	0	32640	32896
19	256	256	65280	65792
20	512	0	130816	131328

Table S1 Combinatorial count of graphene polytypes obeying I Symmetry (no polarization), vertical M symmetry (in-plane polarization only), or no symmetry (in- and out-of-plane polarization)

S2. Measurements Details

S2.1 Raman microscopy

Raman measurements are performed in a commercial WITEC alpha300 Apyron confocal microscope equipped with a UHTS 300 mm focal length spectrometer. We use a 532 nm laser focused down to a spot size of ~300 nm, with a 300 lines/mm grating corresponding to a spectral range of ~3800 cm^{-1} and a spectral resolution of ~ 4 cm^{-1}. The G (~1580 cm^{-1}) and 2D (~2700 cm^{-1}) peaks are taken in a single scan (Fig. 2b). The raster scans are obtained by using a step size of 200 nm, an average power of ~4 mW, and integration times shorter than 1 sec to avoid laser-induced heating.

To construct the Raman maps (Fig 2, Fig S1) we integrate the photon counts in a specific range that optimizes the contrast between polytypes. The filter range of the maps is shown in panel b and c next to it. We note that no damage or boundary wall movements are observed during the scans.

S2.2 AFM measurements

The topography and KPFM measurements are performed using two separate microscopes: (i) PARK

NX-10 in ambient conditions, and (ii) PARK NX-HIVAC in a nitrogen gas environment at a pressure of 100 mbar. We use a PPP-EFM metal-coated tip with a mechanical resonance frequency of ~75 kHz and a spring constant of 3 N/m. The cantilever amplitude at the non-contact modes ranged between 10 and 30 nm. The topography and KPFM signals are obtained separately using a two-pass measurement. The first pass records the topography. In the second pass, the KPFM (DC) potential is recorded by lifting the tip an extra 7 nm and repeating the topography profile of the first pass under a bias voltage of 1.5V AC: 1.5-3 kHz. The side-band KPFM mode is used to obtain a better-defined local potential. We have verified that the surface potentials do not depend on the tip height in the range of 4 to 40 nm above the surface.

We find variations of ~ 200 mV in the average flake potential across different samples, microscopes, and tips. We attribute these variations to different environmental conditions, the charging of the substrate, and tip contaminations. Our conclusions, however, rely only on local surface potential differences between adjacent polytypes, which we find to be independent of all the above-mentioned factors.

We further note that there is a slight potential gradient within each map (a nearly linear variation of a couple of mV over a 10 μm scale), which we attribute to non-local interactions with the macroscopic cantilever. This low-frequency variation is eliminated by standard image processing tools (Gwyddion software).

While clearly detected in line cuts (Fig. 2e, Fig S1), the surface potential above each polytype is quantified more accurately by considering the potential of all the relevant pixels in each polytype region. Indeed, plotting the potential histogram of the adjacent polytypes (after masking out regions of local contaminations) allows us to detect the mean surface potential of a polytype to within ~1 mV.

S3. Additional experimental results

S3.1 Polarization measurements in adjacent polytypes

In total, we identified and characterized nine different tetra-layer graphene flakes, each containing one or more polar polytypes. We note that only a small fraction of the exfoliated flakes, ~ 5%, include a polar polytype. Altogether, these nine flakes included 19 polar polytypes (ten domains pointing up and nine pointing down). Within each flake the different polytypes P, R and B exhibit consistent surface potential differences: $(V_{KP}(P_\uparrow) - V_{KP}(P_\downarrow))/2 = 6\pm1$mV, $V_{KP}(R) - V_{KP}(B) = 19\pm1$mV, $V_{KP}(R) - V_{KP}(P_\uparrow) = 5\pm1$mV, as discussed in the main text.

The polytypes are distinguished by filtering the Raman counts near the 2D or G peaks, as shown in Fig. S1; Interestingly, the region marked by a solid line frame in the figure, which is presented with high resolution in panel (c), contains the two oppositely polarized domains separated by a single domain wall.

Figure S1| Additional samples demonstrating polar domains of opposite polarization. a. Optical image, Raman map, and a surface potential map of a selected tetralayer flake. The Raman map is constructed using a filter near the 2D peak as shown in panel (c). **b/c.** Zoom-in maps on the region framed with a dashed/solid line in both the Raman and surface potential maps of (a). The zoomed-in Raman map is constructed using a filter near the G or 2D peak, noted by a gray bar in the panels. The two domains of the polar polytype (blue arrows) appear in the same color in the Raman maps, but show distinct colors in the surface potential maps. The normalized histogram of the number of pixels per a given surface potential, for each of the polytypes, is fitted with a gaussian curve. Curves of opposite P polytypes are separated by 13 mV in both frames. A further potential line-cut is shown in (c) across the adjacent oppositely polarized domains.

5
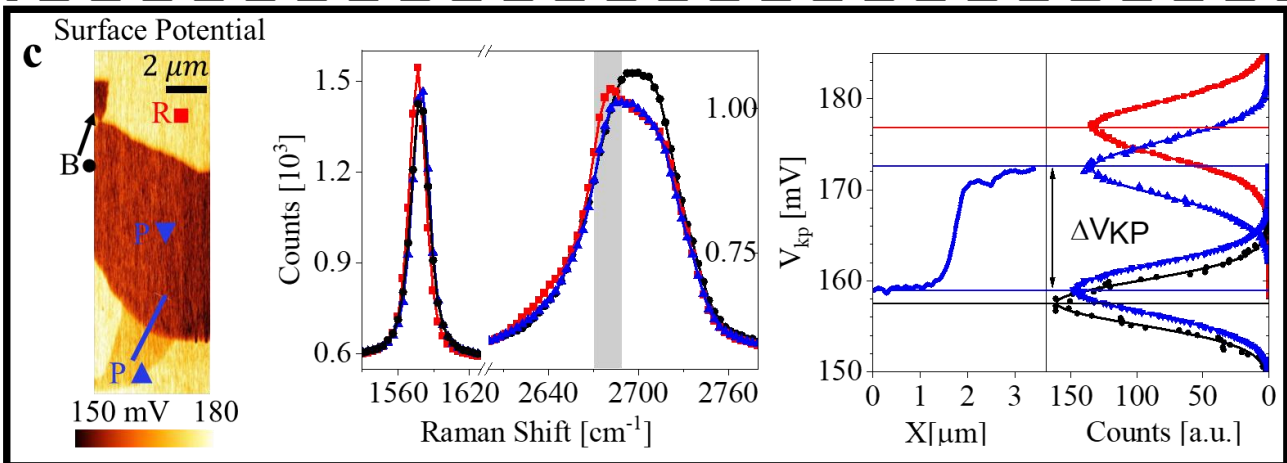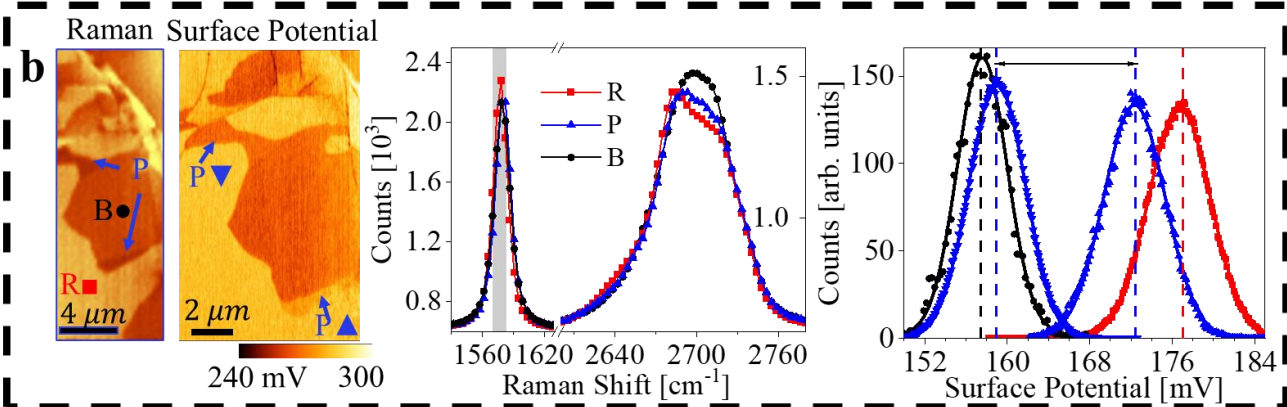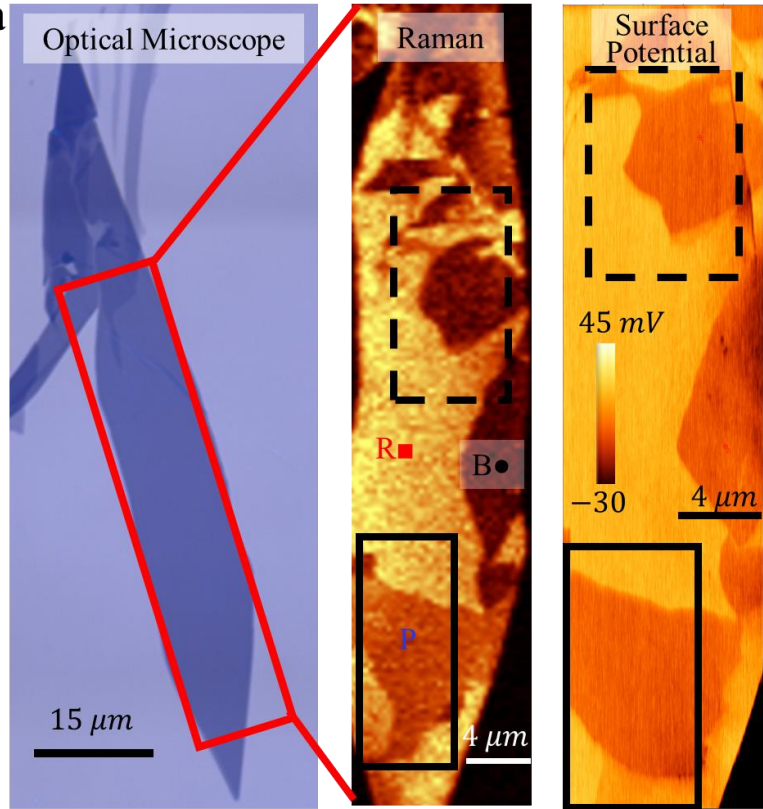
S3.2 Polarization measurements as a function of doping

In the doping-dependent measurements, we apply a gate voltage between the bottom silicon electrode and the graphene, as shown in Figure 2 of the main text. We estimate the charge density from the planar plate capacitance as $n/V_g = \frac{\epsilon_0 \cdot \epsilon_K}{e \cdot d} = 2.3 \times 10^{11} \ cm^{-2}V^{-1}$. In all 9 samples we measured the intrinsic doping to be less than $5 \times 10^{11} \ cm^{-2}$ as expected for freshly exfoliated flakes a clean SiO_2 surface, that experience no polymers nor solvents, and measured under inert conditions. This was confirmed by measuring the V_{KP} gate dependence, which has an antisymmetric response around n=0[1], and the Raman shape and position of the G and 2D peak[2–4]. While several flakes had a monolayer/bilayer sections for which the asymmetric KPFM and the Ramman shift are more pronounced with doping allowing us accurate measurement of the intrinsic doping, for flakes with only thick structure we are limited to an error of $\Delta n = \pm 5 \times 10^{11} \ cm^{-2}$. In figure S2, for example, the antisymmetric KPFM signal indicates and intrinsic hole doping of $5 \times 10^{11} \ cm^{-2}$.

As expected, the potential atop the silicon surface changes according to the applied voltage (in the range of ± 10 V), while above the tetra-layer graphenes, V_{KP} changes by ± 15 mV over the same V_g range (Figure S2). We attribute the latter potential shift observed in all polytypes to the density-dependent Fermi energy and its impact on the work function. The polarization magnitude as a function of V_g and n is extracted from the potential difference between oppositely polarized domains (of otherwise the same material and work function).
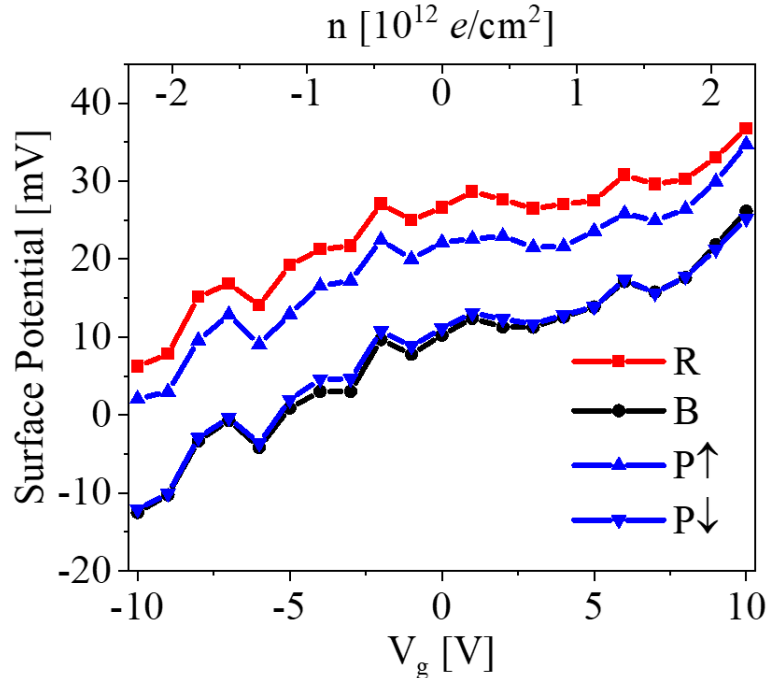

Figure S2| Surface potential variations as a function of gate voltage for the rhombohedral (R), Bernal (B), and two oppositely polarized polar domains (P) tetra-layer polytypes at room temperature.

S4 Theoretical modeling

S4.1 DFT

S4.1.1 Calculation of potential profiles in graphene polytypes

<u>Computational details</u>
The laterally integrated electrostatic potential profiles along the normal direction of three polytypes of four-layered graphene are shown in Fig. 3b of the main text. To obtain the profiles, we used the Perdew-Burke-Ernzerhof (PBE) generalized-gradient exchange-correlation density functional approximation[5], augmented by the Grimme-D3 dispersion correction using Becke-Johnson (BJ) damping[6], as implemented in the Vienna Ab-initio Simulation Package (VASP)[7]. A plane wave energy cutoff of 900 eV and a k-point mesh of $90 \times 90 \times 1$ were used, with a vertical vacuum size of 5 nm to avoid interactions between adjacent images. The core electrons of the carbon atoms were treated via the projector augmented wave (PAW) approach.

The polytypes have been constructed by stacking four relaxed monolayers in the B, R, and P configurations, and further relaxing the entire stack using the conjugated gradients algorithm with a force threshold of 10^{-3} eV/Å. Single-point electron density calculations were then performed on the relaxed structure using a Gaussian smearing of 25.8 meV, to enhance the convergence of the self-consistent cycle.

<u>Consistency and convergence tests</u>
To evaluate the vertical polarization, a dipole moment correction was employed[8]. For validation purposes, double supercell calculations were also performed (see Fig. S3a), where the supercell consists of two opposing mirror images of each graphene stack with a 6 nm inter-image vacuum region with enhanced cutoff and vacuum settings of 1000 eV and 10 nm, respectively, was used. The same enhanced settings were used in Figs. S5 and S6 below. Fig. S3b shows that the dipole correction and double supercell methods yield nearly identical potential profiles with an overall electrostatic potential drop of 6.7 meV.

Convergence tests of the VASP calculations (Fig. S4) indicate that our choice of parameters leads to electrostatic potential differences convergence to within ~0.1-0.2 meV with respect to the number of k-points, energy cut-off, and vacuum size. The same figure shows that even with a relatively dense mesh of 721 k-points the result is only converged to ~0.26 meV, namely, in this case the overall convergence is limited by the k-point sampling.
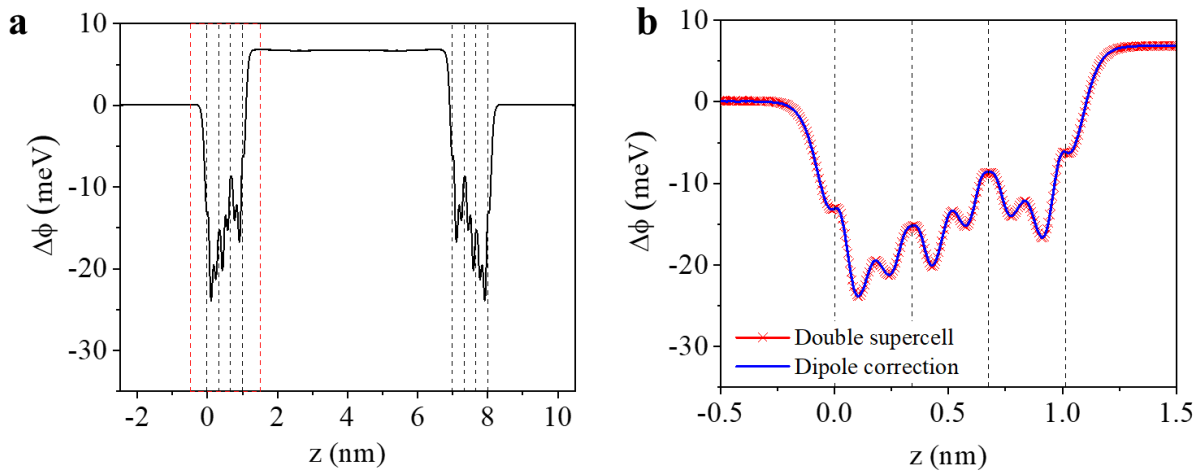
Figure S3. **Potential profiles for a P polytype tetra-layered graphene stack.** (a) Difference between the laterally averaged potential profile obtained for the four-layered graphene stack double supercell and that obtained from a superposition of the corresponding non-interacting monolayers. (b) Comparison between the potential profiles obtained using the dipole correction (blue), and the double supercell method (red), in the dashed-red rectangular region denoted in panel (a). The black dashed lines represent the vertical locations of the four layers. The origin of the horizontal axis is set to the bottom layer.
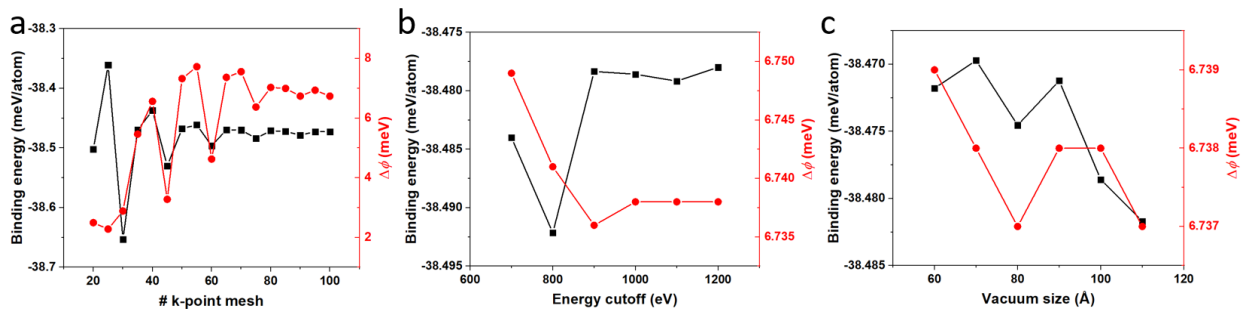

Figure S4. **VASP calculations convergence tests.** Convergence tests of the binding energy (black curve, left vertical axes) and electrostatic potential difference across the entire structure (red curve, right vertical axes) for the P polytype of a four-layered graphene stack with respect to: (a) number of k-points along each one of the two laterally periodic directions; (b) energy cutoff, and (c) vacuum size.

Charge redistribution analysis

The origin of the observed vertical polarization can be traced back to charge redistribution in the non-centrosymmetric polytypes. This is demonstrated in Fig. S5, where charge redistribution and potential difference maps for a 2d cross-sectional cut along the armchair direction ((110) surface) of three polytypes is presented. The variation map is obtained from the difference between the charge density

of the four-layered stack and the super-imposed densities of the corresponding isolated monolayers. The charge density difference map of the P polytype is clearly non-centrosymmetric (Fig. S5a), demonstrating a relatively pronounced in-plane dipolar pattern on the third layer with opposite weaker patterns on the first and fourth layers. Similar but centrosymmetric patterns are found for the R (Fig. S5b) and B (Fig. S5c) polytypes, where the dipolar structure of the former is mainly localized at the edge layers and that of the latter is more pronounced on the middle layers. The corresponding electrostatic potential differences also manifest the broken symmetry of the P polytype (Fig. S5d), and the centrosymmetry of R (Fig. S5e) and B (Fig. S5f) polytypes.
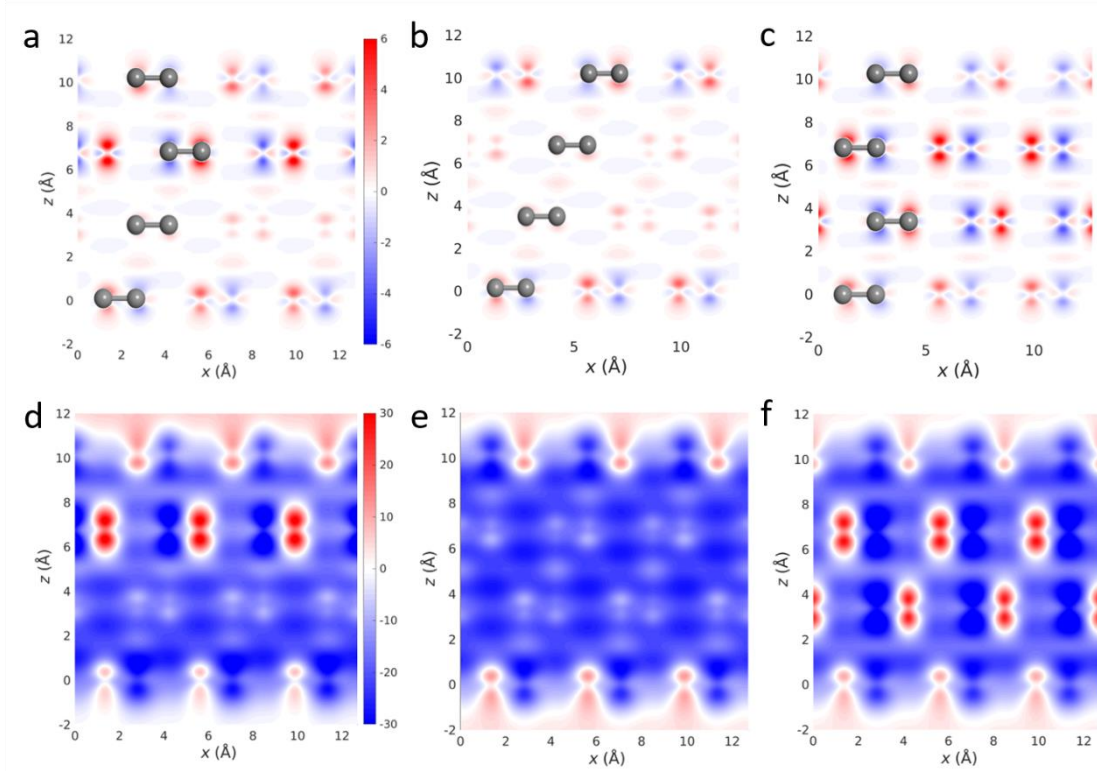

Fig. S5. **Charge redistribution and potential difference maps**. A two-dimensional cross section through the (a)-(c) charge density differences (with respect to the individual monolayers) and (d)-(f) potential difference along the (110) crystallographic plane of the P (a, d), R (b, e) and B (c, f) four-layered graphene polytypes. The scale-bar units for the charge density and potential difference maps are e/nm^3 and meV, respectively. The gray spheres appearing in the upper panels represent the positions of the carbon atoms.

Band structures of the B and R phases

In Fig. 3 of the main text we provide the calculated band-structure of the P polytype to analyze the origin of the observed vertical polarization. For completeness, we present in Fig. S6 the corresponding band structures of the B and R polytypes calculated at the level of theory described above.
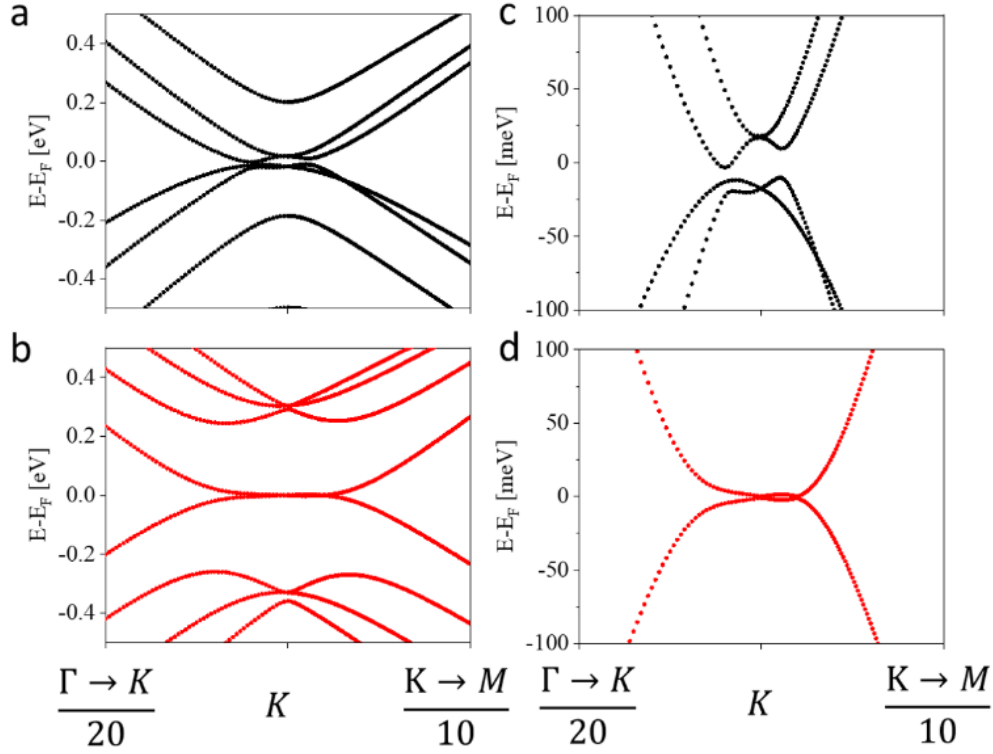
9

Fig. S6. **Band structures**. Calculated band structures of the (a) B, and (b) R, four-layered graphene polytypes. A zoom-in on the energy range near the Fermi energy is given in panels (c) and (d), respectively.

S4.1.2 Calculation of doping dependence of polarization in P polytype graphene

Doping calculations of P polytype four-layered graphene were performed using the fractional nuclear charge pseudoatom approach[9], allowing for simulating doping densities in the experimentally relevant range. To this end, we use pseudopotentials (PPs) generated for atoms with fractional nuclear charge. These calculations were performed using the open-source plane-wave Quantum Espresso package[10] (instead of VASP that was used to perform the calculations described in section S2), allowing us to construct appropriate PPs. We first generated Rappe-Rabe-Kaxiras-Joannopoulos (RRKJ)[11] PPs using the ld1.x program[10 12], while setting the nuclear charge of the carbon pseudoatom to $Z = 6 \pm |\varepsilon|$, the original charge of the neutral element plus a small fractional charge $|\varepsilon|$. The valence electronic charge was changed accordingly to maintain neutrality of the unit-cell, with an electron configuration given by $[He]2s^2 2p^{2\pm\varepsilon}$. A set of PPs were generated by setting $\varepsilon = 10^{-9}, 10^{-8}, ..., 10^{-4}$ for all C atoms in the system, corresponding to doping densities of $\Delta n_{2D} = 1.5 \times 10^7, 1.5 \times 10^8, ..., 1.5 \times 10^{12}$ cm^{-2}, respectively.

Single point calculations were performed using the generated PPs to obtain the electron density and the corresponding electrostatic potential profiles. To this end, we employed the PBE generalized-gradient density functional approximation[5] and the Grimme-D3 dispersion correction with BJ damping[6], as implemented in Quantum Espresso. A plane wave energy cutoff of 55 Ry was used with a k-mesh of $90 \times 90 \times 1$, and a vertical vacuum size of 4 nm was set to avoid interactions between adjacent bilayer images. Fermi-Dirac smearing with an effective temperature of ~300 K was used to

enhance the convergence of the self-consistent cycle. To obtain converged electrostatic potential profiles, a dipole correction was used[8]. Similar to section S4.1.1, we also compared the results against calculations using a double supercell, confirming the consistency of our results (see Fig. S7). As above, enhanced settings of 60 Ry cutoff and 10 nm vacuum were used here and in Figs. S9-S10 below.

As in the procedure discussed in section S4.1.1, undoped P polytype graphene was first constructed and optimized using the Quantum Espresso package, yielding an electrostatic potential drop of 5.4 meV. This value is somewhat smaller than the value of 6.7 meV obtained using VASP (see section S4.1.1), likely reflecting the different pseudopotentials used and other differences in numerical settings. Note, however, that the difference is of the order of 1 meV, which would normally have been considered as very small and only somewhat stands out because the overall dipole is small.
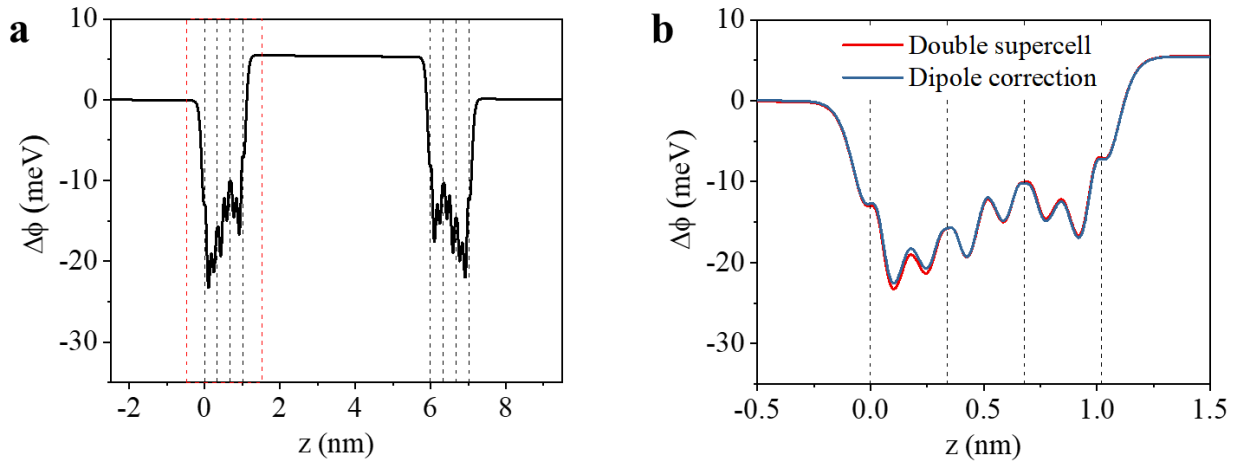

Figure S7. Quantum Espresso potential profiles for a P polytype tetra-layered graphene stack. (a) Difference between the laterally averaged potential profile obtained for the four-layered graphene stack double supercell and that obtained from a superposition of the corresponding non-interacting monolayers. (b) Comparison between the potential profiles obtained using the dipole correction (blue), and the double supercell method(red), in the dashed-red rectangular region denoted in panel (a). The black dashed lines represent the vertical locations of the four layers. The origin of the horizontal axis is set to the bottom layer.

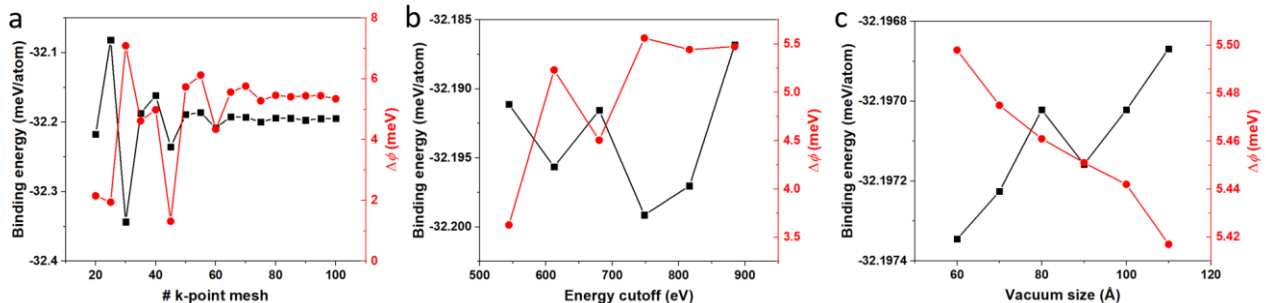**Figure S8. Quantum Espresso calculations convergence tests.** Convergence tests of the binding energy (black curve, left vertical axes) and electrostatic potential difference (red curve, right vertical axes) for the P polytype of a four-layered graphene stack with respect to: (a) number of k-points along each one of the two laterally periodic directions ; (b) energy cutoff, and (c) vacuum size.

Convergence tests of the Quantum Espresso calculations (Fig. S8) indicate that overall convergence to within ~0.2 meV is obtained also for these calculations.
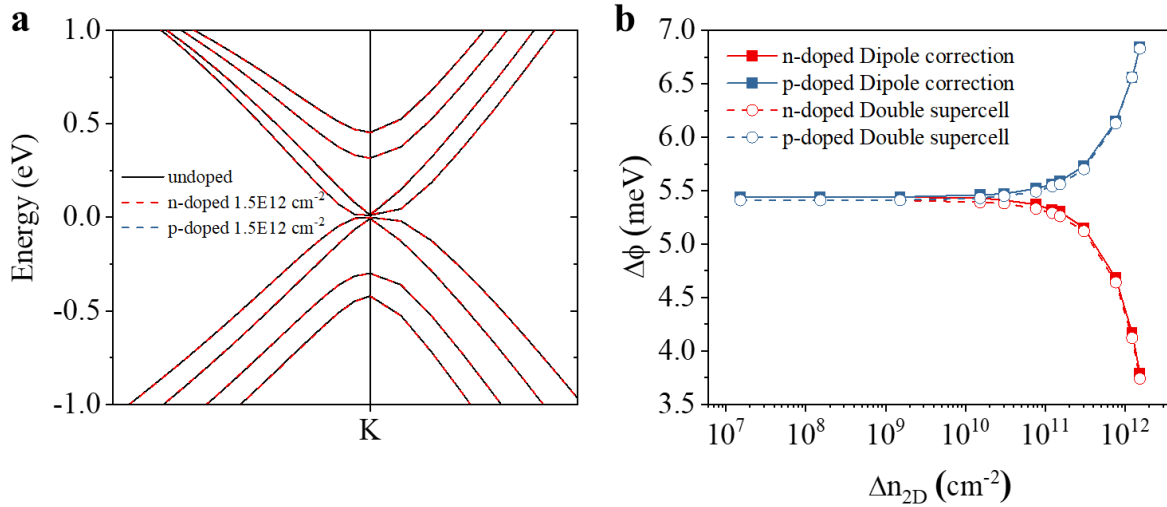

Figure S9. **Effect of doping on the band structure and potential drop.** (a) The band structures of undoped (black) and 1.5×10^{12} cm^{-2} n-(red) and p-(blue) doped P polytype graphene. The origin of the vertical axis is set to the topmost K-point valence band energy. (b) Potential drop as a function of electron (n, red) and hole (p, blue) doping densities, calculated using the dipole correction (solid curves, squares) and the double supercell (dashed curves, circles) methods.

We note that the fractional nuclear charge pseudoatom doping approach[11] adopted in this study remains valid as long as variations in the calculated band-structure, induced by the nuclear pseudo charging, are negligible. To confirm that our calculations satisfy this condition, we compare the band-structures of the undoped and doped cases up to the highest doping density considered (see Fig. S9a). Our results clearly demonstrate merely minor deviations of the band-structures of the doped systems from those of the undoped counterparts. The energy difference between the topmost K and Γ valence band points for the doped and undoped systems (< 0.1 meV) is sufficiently small to be neglected. Upon doping, the polarization remains mostly unaffected up to a threshold value of ~10^{10} cm^{-2}, above which a polarization decrease (increase) is clearly seen for n-(p-)doping (see Fig. S9b). Notably, the dipole correction and the double supercell approaches generate nearly identical doping induced polarization profiles, indicating the reliability of our results.
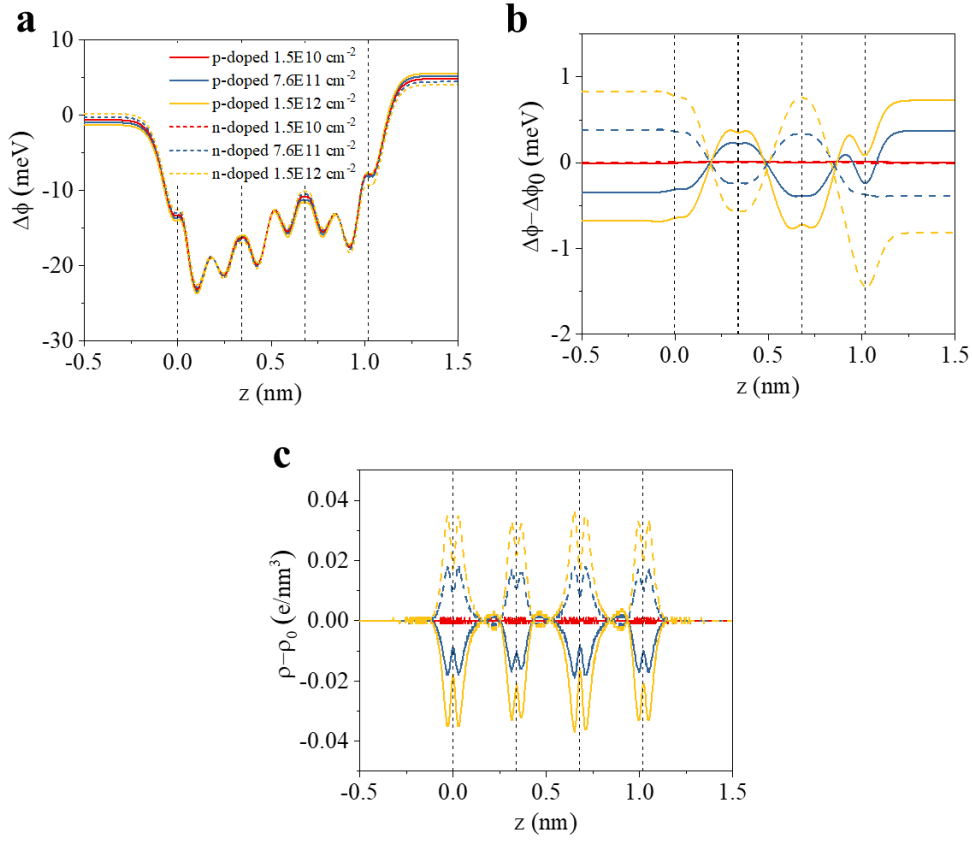
Figure S10. **Doping-induced charge and potential variations.** (a) Laterally averaged vertical potential profiles obtained at p- (solid lines) and n- (dashed lines) doping densities of $1.5 \times 10^{10} \text{cm}^{-2}$ (red), $7.6 \times 10^{11} \text{cm}^{-2}$ (blue), and $1.5 \times 10^{12} \text{cm}^{-2}$ (yellow) after subtracting the superposition of potential profiles of the corresponding monolayers. (b) Doping induced variation of the vertical potential profiles. (c) Doping induced variations of the laterally averaged charge density.

In the main text, we explore the origin of the doping induced polarization variations in terms of the projection of the electronic density of states on the different layers. For completeness, we discuss below how the corresponding potential profile variations are manifested in the charge density redistribution. Fig. S10a shows the laterally-averaged vertical potential profiles (after subtracting the potential profiles of the corresponding non-interacting monolayers) for doping densities near and above the threshold value, demonstrating a somewhat different response of the various layers. A clearer picture is obtained when subtracting the profile of the undoped system (Fig. S10b) showing a strong positive response of the first and third layers, a strong negative response of the fourth layer and a weaker negative response of the second layer. This asymmetric response is also manifested in the laterally averaged charge density difference profiles (Fig. S10c), demonstrating somewhat larger charge variations on the first and third layers, as compared to the second and fourth layers above the threshold doping value.

The tight-binding model of the few-layer graphene is based on a single-particle $\vec{k}$-dependent tight-binding Hamiltonian with a unit cell comprised of two sites per layer, one for the A-sublattice and one for the B-sublattice of single-layer graphene, giving eight total sites for tetralayer graphene (see Fig. S11). The in-plane carbon-carbon and inter-layer distances are taken as $a = 1.42\,\text{Å}$ and $c = 3.4\,\text{Å}$, respectively.

We include on-site potential terms Δ, Δ' on single (e.g. A2) and doubly (e.g. A3) eclipsed sites, respectively. Hopping parameters γ_0

Figure S11| Layout of the tight-binding model.

through γ_5, defined in Fig. 1d of the main text, are taken into account. An in-plane next-nearest-neighbor hopping parameter, t', has also been considered. However, it does not involve inter-sublattice mixing and was found to have a minor effect on the polarization. Thus, although it is present in the form of the Hamiltonian given below, practically it was set to zero.
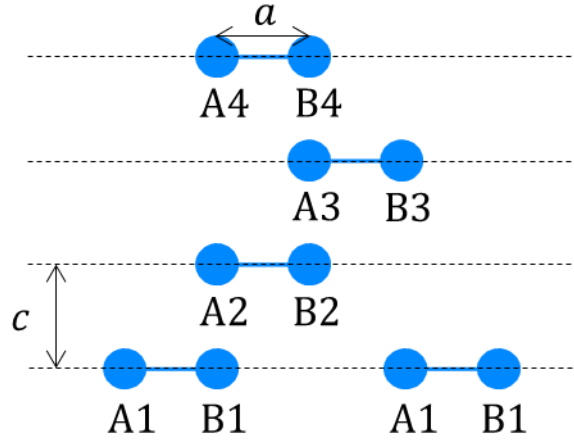
The explicit $\vec{k}$-dependent Hamiltonian matrix for the four-layer polar configuration is given by:

$$
\begin{pmatrix}
t'T(\vec{k}) & \gamma_0 S(\vec{k}) & \gamma_4 S(\vec{k}) & \gamma_3 S^*(\vec{k}) & 0 & \gamma_{2,R} & 0 & 0 \\
\gamma_0 S^*(\vec{k}) & \Delta + t'T(\vec{k}) & \gamma_1 & \gamma_4 S(\vec{k}) & 0 & 0 & 0 & 0 \\
\gamma_4 S^*(\vec{k}) & \gamma_1 & \Delta + t'T(\vec{k}) & \gamma_0 S(\vec{k}) & \gamma_4 S(\vec{k}) & \gamma_3 S^*(\vec{k}) & \gamma_{2,B} & 0 \\
\gamma_3 S(\vec{k}) & \gamma_4 S^*(\vec{k}) & \gamma_0 S^*(\vec{k}) & \Delta + t'T(\vec{k}) & \gamma_1 & \gamma_4 S(\vec{k}) & 0 & \gamma_5 \\
0 & 0 & \gamma_4 S^*(\vec{k}) & \gamma_1 & \Delta' + t'T(\vec{k}) & \gamma_0 S(\vec{k}) & \gamma_4 S^*(\vec{k}) & \gamma_1 \\
\gamma_{2,R} & 0 & \gamma_3 S(\vec{k}) & \gamma_4 S^*(\vec{k}) & \gamma_0 S^*(\vec{k}) & t'T(\vec{k}) & \gamma_3 S(\vec{k}) & \gamma_4 S^*(\vec{k}) \\
0 & 0 & \gamma_{2,B} & 0 & \gamma_4 S(\vec{k}) & \gamma_3 S^*(\vec{k}) & t'T(\vec{k}) & \gamma_0 S(\vec{k}) \\
0 & 0 & 0 & \gamma_5 & \gamma_1 & \gamma_4 S(\vec{k}) & \gamma_0 S^*(\vec{k}) & \Delta + t'T(\vec{k})
\end{pmatrix},
$$

where $S(\vec{k})$ and $T(\vec{k})$ are given by:

$$
S(\vec{k}) = 2e^{ia\frac{k_x}{2}} \cos\left(\frac{\sqrt{3}}{2} a k_y\right) + e^{-iak_x}
$$

$$
T(\vec{k}) = 2\cos(\sqrt{3}ak_y) + 4\cos\left(\frac{3}{2}ak_x\right)\cos\left(\frac{\sqrt{3}}{2}ak_y\right)
$$

Parameter	Δ	Δ'	γ_0	γ_1	$\gamma_{2,R}$	$\gamma_{2,B}$	γ_3	γ_4	γ_5	t'
Value (eV)	-0.008	-0.016	3.16	0.39	-0.02	-0.02	0.315	0.044	0.038	0

Table S2| Numerical values of parameters used in the tight-binding model based on Ref. [13].

The Hamiltonian is then diagonalized to calculate the energy and the electron distribution across the unit cell sites of each state. In order to calculate the overall polarization for a given chemical potential and temperature, the different states are populated according to a Fermi-Dirac distribution. The electron distribution is then numerically integrated across the entire Brillouin Zone and all bands (accounting for spin degeneracy) to obtain the total electron occupation of each site. The polarization voltage in the out-of-plane direction is extracted by weighing each site occupancy by the corresponding vertical position from the center of the structure, assuming point-like orbitals.

Self-consistent treatment of the Coulomb Interaction

In order to account for the electrostatic interactions resulting from the non-uniform distribution of charge, a self-consistent approach is employed. Given a total charge distribution, it is possible to calculate the electrostatic potential differences between the different sites of the unit-cell. These potential differences may then be re-inserted into the single-particle Hamiltonian as on-site potentials. Since only potential differences have physical meaning, the inserted on-site potentials are always shifted such that they sum up to zero. The modified Hamiltonian is then solved to extract an updated charge distribution, with corresponding electrostatic potential differences. Using a nonlinear solver, a self-consistent set of potentials is found.

In general, the on-site potentials arising from the charge distribution can be expressed as $V_i = \sum_j G_{ij} n_j$, where V_i is the on-site potential at site $i = A1, \cdots, B4$ (and similarly for j, see Fig. S11), n_i is the corresponding excess charge, and G_{ij} is an interaction matrix. Two different models were tested for the purpose of calculating the interaction matrix: A plate capacitor model and an Ewald summation model. Let us describe each in turn.

Plate capacitor model:

In the plate capacitor model, the overall charge of each layer, including the positive ions, is calculated based on the electron distribution. Each layer is treated as a uniformly charged capacitor plate of infinite dimensions, with a charge density equal to the total charge of a unit cell divided by its area. The potential differences between the different layers is then readily calculated. Explicitly, the interaction matrix for this model is given by:

$$G_{ij} = -|l(i) - l(j)| \frac{c}{2\varepsilon_0 A},$$

where ε_0 is the permittivity of free space, $A = \frac{3\sqrt{3}}{2} a^2$ is the unit-cell area, and $l(i) = 1, \cdots, 4$ is the layer index of lattice site i.

Ewald Summation model:

In this approach, the two-dimensional Ewald summation approach[14] is used to calculate the potentials in each lattice site, as generated by the net charge of all other sites in the infinite two-dimensional lattice, assuming point-like orbitals. The value of the cutoff parameter[14] was chosen to be $\xi = 0.4\sqrt{A}$, with A being the unit cell area. We note, however, that different choices of this parameter had a negligible effect on the result.

Because Ewald summation is only valid when the net-charge of the unit cell is zero, any net charge of the distribution must be counteracted by uniformly adjusting the charge of the carbon ions such that the net charge is zero, as done also in the DFT calculations. We have verified that modelling the effect of the gate electrode by means of placing the extra charge on an external gate layer did not modify the results in any significant way.

Because the Ewald summation does not account for self-interaction energy within a lattice site, the chemical hardness of carbon[15] was modelled by adding a fixed value of $\eta = 10.0\ eV$ [15] on top of the electrostatic potential generated by all other lattice sites. Explicitly, the interaction matrix for this model is then given by:

$$G_{ij} = G_{ij}^0 + \eta \delta_{ij},$$

where δ_{ij} is the Kronecker delta and the numerical values of G_{ij}^0 are given (in units of [V/e]) by:

$$
\begin{pmatrix}
-24.65 & -9.02 & -58.67 & -58.67 & -117.33 & -117.33 & -176.00 & -176.00 \\
-9.02 & -24.65 & -58.67 & -58.67 & -117.33 & -117.33 & -176.00 & -176.00 \\
-58.67 & -58.67 & -24.65 & -9.02 & -58.67 & -58.67 & -117.33 & -117.33 \\
-58.67 & -58.67 & -9.02 & -24.65 & -58.67 & -58.67 & -117.33 & -117.33 \\
-117.33 & -117.33 & -58.67 & -58.67 & -24.65 & -9.02 & -58.67 & -58.67 \\
-117.33 & -117.33 & -58.67 & -58.67 & -9.02 & -24.65 & -58.67 & -58.67 \\
-176.00 & -176.00 & -117.33 & -117.33 & -58.67 & -58.67 & -24.65 & -9.02 \\
-176.00 & -176.00 & -117.33 & -117.33 & -58.67 & -58.67 & -9.02 & -24.65
\end{pmatrix}.
$$

For sites in different layers the values are very similar to the corresponding plate-capacitor ones. The main difference between the two models is in the intra-layer interactions, as discussed further below.

Results and discussion

In Figure S12 we compare the results of the different models for introducing a self-consistent electrostatic potential to the TB Hamiltonian: (i) none; (ii) plate capacitor model; and (iii) Ewald summation. When the self-consistent potential is neglected the polarization tends to be rather large. The self-consistent inclusion of the interaction strongly reduces the polarization value and may even flip its sign. The main difference between the plate capacitor and Ewald models is in the behavior of the polarization of the flat bands. Those bands, inherited from the Rhombohedral bottom 3 layers, reside mainly at the sites A1 and B3 [16]. At the K point and without the self-consistent potentials, only the $\gamma_{2,R}$ hopping amplitude is important, leading to bonding and antibonding eigenstates, the mean vertical position of which is close to layer 2. This behaviour holds also in the plate capacitor model. Only with Ewald summation, which allows for intra-layer potential difference, can the onsite potentials difference between A1 and B3 become sufficiently large with respect to $\gamma_{2,R}$. This then cause the eigenstates to reside mainly at one site or the other, as in the DFT calculation, which is important for obtaining both the right value of the polarization at charge neutrality and its doping dependence. Note that the trigonal warping caused by $\gamma_{3,4}$ leads to the gap between these two bands nearly closing away from the K point, a feature not seen in the DFT calculations, though without much effect on the polarization.

As for the low-energy Dirac bands, these are borne out of the Bernal top 3 layers. One of them mainly resides at site A4 and the other at an anti-bonding combination of B4 and B2 [16]. Their location and

separation are thus determined by the combined effect of γ_5, Δ, and the self-consistent electrostatic potential, and hence are quite sensitive to the parameter values. Only the Ewald model gives rise to a relatively symmetric bandstructure that is reminiscent of the DFT results.
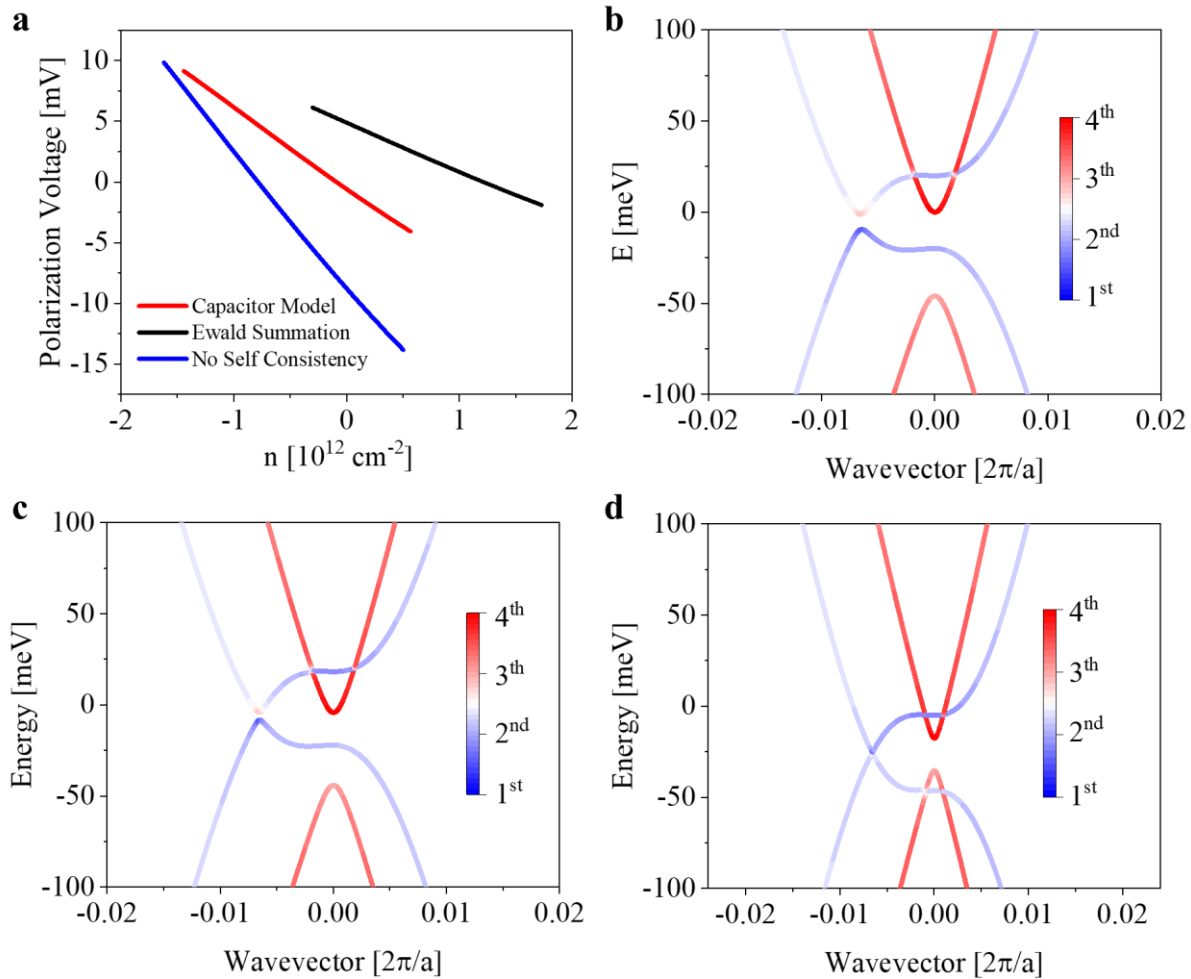

Figure S12| Comparison of the different models of including electrostatic interactions in the TB calculation. (a) Doping dependence of the polarization at room temperature. (b)-(d) near Fermi-level band structures, around the K point as in Fig. 3 of the main text. (b) No electrostatic interaction, (c) plate capacitor model, (d) Ewald summation model.

References

1.   Yu, Y.-J. *et al.* Tuning the Graphene Work Function by Electric Field Effect. *Nano Lett.* **9**, 3430–3434 (2009).
2.   Yan, J., Zhang, Y., Kim, P. & Pinczuk, A. Electric field effect tuning of electron-phonon coupling in graphene. *Phys. Rev. Lett.* **98**, (2007).
3.   Pisana, S. *et al.* Breakdown of the adiabatic Born-Oppenheimer approximation in graphene. *Nat. Mater.* **6**, 198–201 (2007).
4.   Bruna, M. *et al.* Doping dependence of the Raman spectrum of defected graphene. *ACS Nano* **8**, 7432–7441 (2014).
5.   Perdew, J. P., Burke, K. & Ernzerhof, M. Generalized gradient approximation made simple. *Phys. Rev. Lett.* **77**, 3865–3868 (1996).
6.   Grimme, S., Antony, J., Ehrlich, S. & Krieg, H. A consistent and accurate ab initio parametrization of density functional dispersion correction (DFT-D) for the 94 elements H-Pu. *J. Chem. Phys.* **132**, 154104 (2010).
7.   Kresse, G. & Furthmüller, J. Efficient iterative schemes for ab initio total-energy calculations using a plane-wave basis set. *Phys. Rev. B - Condens. Matter Mater. Phys.* **54**, 11169–11186 (1996).
8.   Makov, G. & Payne, M. C. Periodic boundary conditions in ab initio calculations. *Phys. Rev. B* **51**, 4014–4022 (1995).
9.   Sinai, O. & Kronik, L. Simulated doping of Si from first principles using pseudoatoms. *Phys. Rev. B - Condens. Matter Mater. Phys.* **87**, 235305 (2013).
10.   Giannozzi, P. *et al.* QUANTUM ESPRESSO: A modular and open-source software project for quantum simulations of materials. *J. Phys. Condens. Matter* **21**, 395502 (2009).
11.   Rappe, A. M., Rabe, K. M., Kaxiras, E. & Joannopoulos, J. D. Optimized pseudopotentials. *Phys. Rev. B* **41**, 1227–1230 (1990).
12.   Dal Corso, A. Pseudopotentials periodic table: From H to Pu. *Comput. Mater. Sci.* **95**, 337–350 (2014).
13.   Dresselhaus, M. S. & Dresselhaus, G. Intercalation compounds of graphite. *Adv. Phys.* **30**, 139–326 (1981).
14.   Harris, F. E. Ewald summations in systems with two-dimensional periodicity. *Int. J. Quantum Chem.* **68**, 385–404 (1998).
15.   Franco-Pérez, M. & Gázquez, J. L. Electronegativities of Pauling and Mulliken in Density Functional Theory. *J. Phys. Chem. A* **123**, 10065–10071 (2019).
16.   Koshino, M. & McCann, E. Multilayer graphenes with mixed stacking structure: Interplay of Bernal and rhombohedral stacking. *Phys. Rev. B - Condens. Matter Mater. Phys.* **87**, 045420 (2013).